

Soft Magnetic Properties and Electromagnetic Shielding Performance of Fe₄₀Ni₄₀B₂₀ Microfibers

Original

Soft Magnetic Properties and Electromagnetic Shielding Performance of Fe₄₀Ni₄₀B₂₀ Microfibers / Sharifikolouei, E; Zywczyk, A; Sarac, B; Koziel, T; Rashidi, R; Bala, P; Fracasso, M; Gerbaldo, R; Ghigo, G; Gozzelino, L; Torsello, D. - In: ADVANCED ELECTRONIC MATERIALS. - ISSN 2199-160X. - (2023). [10.1002/aelm.202300178]

Availability:

This version is available at: 11583/2979952 since: 2023-07-05T15:59:43Z

Publisher:

WILEY

Published

DOI:10.1002/aelm.202300178

Terms of use:

This article is made available under terms and conditions as specified in the corresponding bibliographic description in the repository

Publisher copyright

(Article begins on next page)

Soft Magnetic Properties and Electromagnetic Shielding Performance of $\text{Fe}_{40}\text{Ni}_{40}\text{B}_{20}$ Microfibers

Elham Sharifikolouei,* Antoni Żywczak, Baran Sarac, Tomasz Kozieł, Reza Rashidi, Piotr Bala, Michela Fracasso, Roberto Gerbaldo, Gianluca Ghigo, Laura Gozzelino, and Daniele Torsello

$\text{Fe}_{40}\text{Ni}_{40}\text{B}_{20}$ metallic glass is a key material among the many amorphous systems investigated thus far, owing to its high strength and appealing soft magnetic properties that make it suitable for use as transformer cores. In this study, $\text{Fe}_{40}\text{Ni}_{40}\text{B}_{20}$ microfibers are fabricated down to 5 μm diameter. Three different melt-spinning wheel velocities: $\approx 51 \text{ m s}^{-1}$, $\approx 59 \text{ m s}^{-1}$, and $\approx 63 \text{ m s}^{-1}$ (MG1, MG2, MG3) are used. Their fully amorphous structure is confirmed using X-ray diffraction, and differential scanning calorimetry (DSC) traces reveal a larger relaxation profile for the higher-quenched microfiber. Vibrating sample magnetometer measurements showed a higher saturation magnetization of 136 emu g^{-1} for annealed metallic glass microfibers with a wheel velocity of 59.66 ms^{-1} . Cylindrical magnetic field shields are obtained by aligning and wrapping the fibers around a cast. The observed anisotropic static field shielding behavior is in accordance with the microfibers' anisotropic nature. Composite samples are also produced by embedding the microfibers in an epoxy matrix to investigate their electromagnetic properties at GHz frequencies. Inclusion of the microfibers increase the composite's attenuation constant by 20 to 25 times, making it an ideal candidate for applications in the communications frequency range.

in molding metallic glasses into complex shapes due to localized shear bands that can cause spontaneous failure during plastic deformation.^[2] To overcome this issue, various techniques have been developed, such as additive manufacturing and thermoplastic forming. However, these methods have their limitations and cannot be applied to all metallic glass systems, especially those with marginal glass-forming ability. Thermoplastic molding requires a broad supercooled liquid region (SLR) in the system to avoid crystallization during the heating process, but not all metallic glass systems have a wide SLR. Chemical segregation and oxidation are other challenges associated with this approach. Similarly, additive manufacturing often results in crystallization, with only the surface layer of the substrate being amorphous while the other layers become severely crystalline.^[3] As a result, most metallic glasses produced

1. Introduction

Metallic glass is a highly desirable material due to its exceptional properties, which include corrosion resistance, high elasticity, ultrahigh strength, and soft magnetic properties.^[1] However, conventional casting methods face a long-standing challenge

by additive manufacturing are only partially amorphous and not fully amorphous.^[4]


Metallic fibers are highly desirable for use in flexible and wearable electronics due to their superior properties compared to rigid planar electronics, including flexibility, stretchability, and breathability. Microfibers can be combined to form porous 2D

E. Sharifikolouei, R. Rashidi, M. Fracasso, R. Gerbaldo, G. Ghigo, L. Gozzelino, D. Torsello
 Institute of Materials Physics and Engineering
 Department of Applied Science and Technology
 Politecnico di Torino (POLITO)
 Torino 10129, Italy
 E-mail: elham.sharifikolouei@polito.it

A. Żywczak, T. Kozieł, P. Bala
 Academic Centre for Materials and Nanotechnology (ACMIN)
 Krakow 30-001, Poland

B. Sarac
 Erich Schmid Institute of Materials Science
 Austrian Academy of Sciences
 Leoben 8700, Austria

M. Fracasso, R. Gerbaldo, G. Ghigo, L. Gozzelino, D. Torsello
 Istituto Nazionale di Fisica Nucleare
 Sezione di Torino
 Torino 10125, Italy

 The ORCID identification number(s) for the author(s) of this article can be found under <https://doi.org/10.1002/aelm.202300178>

© 2023 The Authors. Advanced Electronic Materials published by Wiley-VCH GmbH. This is an open access article under the terms of the Creative Commons Attribution License, which permits use, distribution and reproduction in any medium, provided the original work is properly cited.

DOI: 10.1002/aelm.202300178

and 3D structures and easily embedded in various structures, making them suitable for a range of applications, including microelectronics. Metallic glass microfibers, in particular, offer several advantages over thin strips and ribbons, thin films, and composite structures in terms of their magnetic properties. They exhibit smaller hysteresis loss, a near-zero magnetostriction coefficient, and high magnetic permeability, making them ideal candidates for sensitive magnetic sensor systems.^[5] Moreover, metallic glass microfibers have a large specific surface area and significant magnetic anisotropy due to their quasi-one-dimensional structure.^[6] One method for the production of amorphous metal microwires in the range of 100 μm diameter is melt-extraction. This method has been widely used to produce amorphous metallic wires such as Fe–Si–B, Fe–Si–B–M (M = Nb, Ta, Cr, or Mo),^[7] and Co–Si–B.^[8] The magnetic properties and microwave absorbing of Fe-based microwires has been investigated by Jingshun Liu et al.^[9] They concluded that the mass ratio of the Fe-based metallic microwires, sample thickness, and the Ni doping amount have a great influence on the microwave absorbing properties of their composites. In another research conducted by the same group,^[10] they have shown that among Fe-based microwires, the magnetic performance of FeSiBNi₂ is superior but increasing the doping value of Ni and reaching FeSiBNi₃ enhances its mechanical performance reaching the tensile strength of 2518 MPa. Despite the great performance of metallic microwires in terms of magnetic and mechanical properties, as stated earlier, metal wires are in the range of 100–1000 μm diameter, limiting their application in nonwoven textiles or wearable electronics. It is also stated that metallic wires are often stiff and rigid, limiting their applications in wearables that require adequate flexibility and deformability.^[11]

One promising method for fabricating metallic glass microfibers is based on drawing bulk metallic glasses. The outcome of BMG thermoplastic drawing is determined by the processing temperature and the pulling velocity, which affect the viscosity and the strain rate, respectively. The key factor for the successful fabrication of metallic glass microfibers is achieving a balance between the pulling velocity and the temperature, which affects viscosity. If the temperature is too low or the pulling velocity is excessive, the metallic glass demolds itself because the flow stress exceeds the adhesive strength. Conversely, if the temperature is too high, the liquid filament rapidly thins and breaks due to capillary stress. This technique has shown very promising results,^[12] but it is a time-consuming and labor-intensive process that makes it difficult to scale up the production of metal microfibers for large-scale applications. Additionally, it is only suitable for certain metallic glass systems with a broad supercooled liquid region (SLR).

In this study, we utilized a modified melt-spinning technique to fabricate soft magnetic metallic glasses as microfibers, using a recently developed technique that differs from standard fiber fabrication techniques such as bundle drawing. Unlike these techniques, our method does not require plastic deformation to form the fibers.^[13] Instead, the alloy melts directly and forms microfibers via solidification. As a result, this technique can be applied to all metallic glass systems, making it a versatile approach for fabricating metallic glass microfibers.^[14,15]

Fe-based metallic glass systems, as soft magnetic materials, have great potential in applications in electronic information and

green energy vehicles due to their low cost and excellent performance. Fe-rich metallic glasses offer increased saturation magnetic flux density (BS), leading to their utilization for electric appliances and devices.^[16] The FeNiB alloys, depending on iron and nickel concentration and thermal treatment, can crystallize in bcc and/or fcc structures. Often, the Ni-rich phase crystallizes in fcc, such as Ni₃Fe intermetallic compound,^[17] while the Fe-rich phase forms a bcc structure. Alloys with fcc structure exhibit exciting thermal and magnetic properties such as nearly zero thermal expansion coefficient around room temperature, sudden deviation of the saturation magnetization from the Slater–Pauling curve, strong forced volume magnetostriction, low ferromagnetic ordering temperature T_c compared to the T_c of bcc iron and fcc nickel and non-Invar γ -FeNi.^[18]

Numerous studies have been carried out on the magnetic properties of thin films,^[19,20] ribbons,^[21,22] and bulk^[23,24] forms of Fe-based metallic glasses. Two approaches are used to tailor the magnetic properties of glassy alloys: adding the correct alloying elements and annealing the alloy. Wang et al.^[25] developed a Fe-based amorphous structure containing ultra-fine nano α -Fe grains by tuning the composition and quenching regime, leading to softer magnetic properties. Liang et al.^[26] reached a softer alloy by adding Mo, Al, and B to a FeNi-based thin film. Kong et al.^[27] synthesized a Fe–B–Si–P amorphous ribbon with a high saturation magnetization up to 1.7 T and a low coercivity of 3.3–6.2 A m⁻¹. Zhou et al.^[28] reported a very low coercivity of 0.65 A m⁻¹ in a FeNiBSiNbP bulk metallic glass.

The mechanical properties and morphology of magnetic metallic glasses make them appealing for electromagnetic shielding applications, a crucial aspect of device compatibility in several fields. A lot of attention is devoted to the employment of soft magnetic materials for electromagnetic shielding,^[29,30] with works focused both on the development of novel materials^[31] and on the preparation in the form of fibers: stainless steel fibers were investigated,^[32] as well as glass fibers coated with FeCoNi.^[33]

2. Experimental Section

The Fe₄₀Ni₄₀B₂₀ (Fe, Ni, and B >99.9%purity) alloy ingots were synthesized by Arc Melter AM (Edmund Bühler GmbH) using a mixture of elements (with 99.9% or higher purity) under Ti-gettered argon atmosphere. To ensure its homogeneity, ingots were re-melted four times. The ingots were suction-casted in a copper mold with a water-cooled system. The chamber was evacuated to 6×10^{-5} mbar and then filled with high-purity Ar up to 800 mbar. The rods were further used to fabricate Fe₄₀Ni₄₀B₂₀ microfibers through a modified melt-spinning technique. Similar to the standard melt-spinning method, the rod was molten by an induction coil in a BN crucible (18 × 95 mm). The melt was ejected on a rotating copper wheel of different velocities (see Table 1) through a rectangular slit nozzle (10 × 0.03 mm²) (IN-NOVACERA, China) by applying the argon gas pressure on the melt. Unlike the stationary melt-puddle formation in planar flow melt-spinning technique, here, the melt was ejected droplet-by-droplet through the named slit nozzle on a fast-rotating copper wheel. Each droplet wets the rotating copper wheel, and wheel rotation helps the melt create a thin film on the wheel surface. The film spontaneously breaks down into smaller parts and

Table 1. Experimental parameters of Fe₄₀Ni₄₀B₂₀ microfiber fabrication by modified melt-spinning.

Sample	Wheel velocity	Slit nozzle opening	Ejection pressure	Chamber pressure	Ejection temperature	Slit distance to the wheel
Unit	[m s ⁻¹]	[μm]	[mbar]	[mbar]	[K]	[μm]
MG1	51.02	30	1100	400	1623	200
MG2	59.66	30	1500	400	1623	200
MG3	62.8	30	1500	400	1573	200

simultaneously solidifies in the microfiber form due to hole nucleation and growth.

Microstructure analysis was conducted by scanning electron microscopy (SEM) equipped with energy dispersive spectroscopy (EDS, JCM – 6000Plus Versatile Benchtop JEOL, for compositional assessment). The crystallographic structure was investigated by X-ray diffraction with a PANalytical Empyrean X-ray diffractometer with Co K_α radiation ($\lambda = 1.7089 \text{ \AA}$; Co-K_{α1} and Co-K_{α2} radiation filtering) with a step size of 0.026 degrees in θ – 2θ scan mode in Bragg–Brentano geometry. XRD analysis was conducted on samples after DSC measurements which are referred to as “annealed samples”.

Magnetization as a function of temperature from 300 to 1250 K was measured at ACPMIN AGH UST for all samples using a LakeShore Model 7407 vibrating sample magnetometer with an oven in an argon atmosphere (purity 99.9995 percent) with a heating rate of 5 K min⁻¹ in the presence at 0.1 T field. The samples were mounted with Thermeez 7020 ceramic putty on a quartz rod. Curie temperatures T_C were estimated as the maximum of the first derivative of the curve.

The AC electromagnetic properties of MG2 samples embedded in an epoxy matrix (25 wt.%) were measured in the GHz range using a cylindrical coaxial cell (EpsiMu toolkit by Multiwave Innovation, FR^[34]), containing the sample as a spacer between inner and outer conductors, whose diameters are 0.56 and 1.3 cm, respectively, in accordance with the methodology reported by Torsello et al.^[35,36] Two conical parts linked the cell to standard connectors, which helped to keep the characteristic impedance to 50 Ω, thus avoiding mismatch and energy loss. The suitably calibrated cell was connected to a ZVK Vector Network Analyzer (Rohde & Schwarz GMBH & Co, DE, Munich, Ger-

many), and measurements were analyzed with a two-port transmission line technique. The electromagnetic properties of the sample were determined by de-embedding and the Nicolson–Ross–Weir transmission–reflection algorithm.^[37,38] This procedure allowed measuring the complex relative permittivity ϵ and permeability μ of the composites, from which one can calculate the properties of interest for this study: the high frequency conductivity $\sigma = \epsilon_0 \epsilon'' f / 2\pi$ and the attenuation constant of electromagnetic radiation^[39] (Equation 1):

$$\alpha = \frac{\sqrt{2\pi}f}{c} \sqrt{(\mu''\epsilon'' - \mu'\epsilon') + \sqrt{(\mu''\epsilon'' - \mu'\epsilon')^2 + (\mu'\epsilon'' + \mu''\epsilon')^2}} \quad (1)$$

To investigate the static magnetic field shielding performances of tubular screens consisting of a multilayer of superimposed MG2 microfibers, the fibers were pasted on a non-conducting (silicone) cylinder with a height of 27 mm and an external diameter of 21.5 mm. Two different arrangements were analyzed, with the microfibers placed parallel to the cylinder axis or wrapped around the cylinder, henceforth called MG2 vertical and MG2 horizontal configuration, respectively.

The shielding properties of both configurations were investigated by measuring the magnetic flux density in the shield center using a Ga–As Hall probe. The measurements were carried out in both axial and transverse applied field orientations (**Figure 1**) up to an applied field of $B_{app} = 65 \text{ Oe}$. In both directions, the probe was always oriented to measure the component of the magnetic flux density, B_z , parallel to the applied field, as shown in **Figure 1**.

3. Results and Discussion

Figure 2a illustrates a schematic representation of the modified melt-spinning technique used to form metal microfibers. Unlike standard melt-spinning, this modified technique does not involve a stationary melt puddle. Instead, the melt is ejected through a rectangular slit nozzle on the fast-rotating copper wheel as single droplets, forming a thin film. The fast-rotating wheel's centripetal forces and vibrational instability cause the film to break down upon solidification, forming microfibers. This hypothesis is supported by the observation of defective microfibers resulting from unbroken thin films.^[14] The heat pull instantly solidifies upon contact with the copper wheel, and the melt solidifies directly in the form of microfibers.

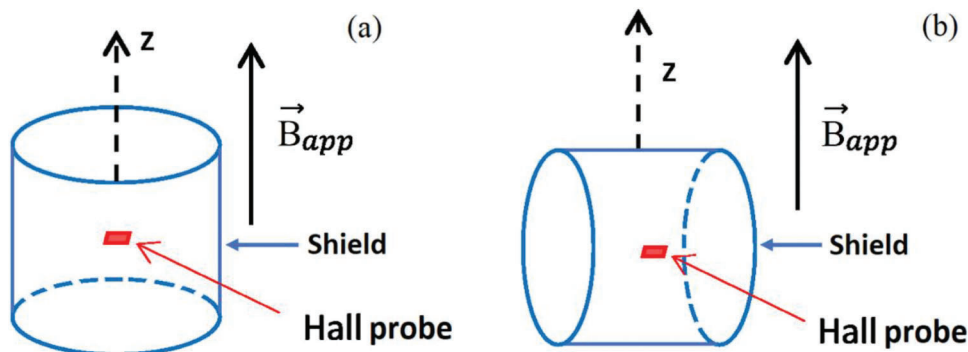


Figure 1. Schematic view of the two arrangements for the shielding measurements in the axial field (a) and transverse field (b) orientation.

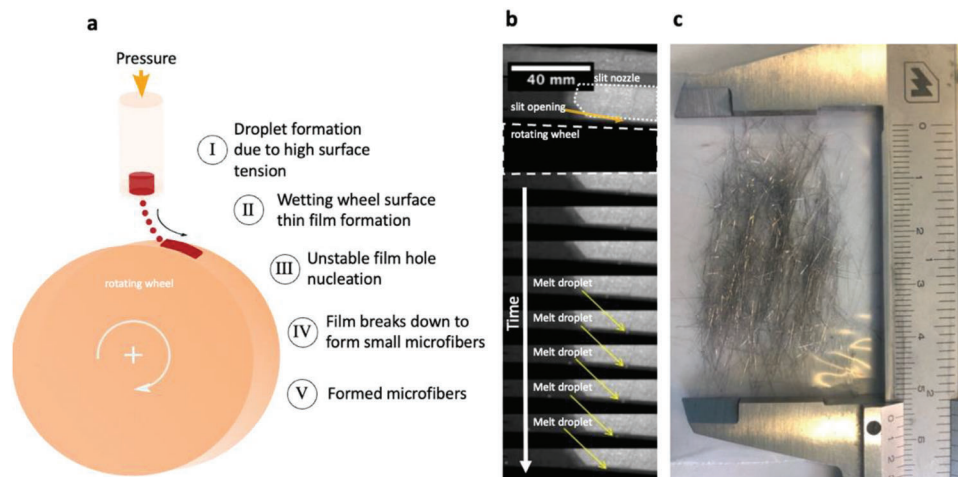


Figure 2. Fabrication of microfibers by modified melt-spinning technique. a) Schematic representation of metal microfiber formation by the modified melt-spinning technique: I) Droplet formation due to high surface tension. II) Wetting wheel surface thin film formation. III) Unstable film hole nucleation. IV) Film breaks down to form small microfibers. V) Formed microfibers. b) Images taken from a high-speed camera movie during the melt-spinning process. c) Fabricated $\text{Fe}_{40}\text{Ni}_{40}\text{B}_{20}$ microfibers. (Part a and b adapted from author's paper,^[14] Springer Nature Limited).

Figure 2b shows the pictures taken by a high-speed camera during the melt ejection. Clearly, no puddle is formed, and each melt droplet is formed and wets the wheel surface individually. The solidified microfibers are shown in Figure 2c. This process offers the advantage of direct microfiber fabrication without additives. Additionally, given the complexity of shaping amorphous metals, amorphous metal microfibers could be utilized further to create porous structures and more complex shapes.

Fabricated $\text{Fe}_{40}\text{Ni}_{40}\text{B}_{20}$ microfibers under different wheel velocities were investigated for their morphology by SEM. Figure 3 shows the SEM images of MG1, MG2, and MG3 microfibers (see Table 1 for the experimental parameters). All microfiber batches have flat-shaped morphology and rectangular cross-sections.

The XRD patterns of as-cast MG1, MG2, and MG3 microfibers were analyzed and found to exhibit a broad diffuse pattern characteristic of an amorphous structure, as shown in Figure 4a. Upon annealing the microfibers at 800 K, XRD analysis revealed the formation of crystals of Ni_3Fe and (Ni,Fe) intermetallic structures, as shown in Figure 4b. The DSC curves of the different samples are shown in Figure 4c, with the characteristic temperatures, including the onset temperature of crystallization (T_x) and the crystallization peak temperature (T_p), listed in Table 2. Though the characteristic temperatures differ slightly, this difference is within the range of experimental error. Therefore, it could be assumed with a good approximation that the characteristic temperatures are constant. The DSC curves of all samples show a single endothermic peak ≈ 700 K. This peak could be related to the eutectic crystallization of $\gamma\text{-Fe-Ni}$ and $(\text{Fe},\text{Ni})_3\text{B}$ phases, as previously reported by Gutfleisch et al.^[40] at 708 K. The area under the crystallization peak is calculated for each sample, and it shows that increasing the wheel velocity from 51.02 to 59.66 m s^{-1} and 62.8 m s^{-1} , the crystallization enthalpy changes from 48, to 62, and 213 $\mu\text{V s}^{-1} \text{mg}^{-1}$, respectively. The shift of the crystallization peaks to higher temperatures can be attributed to the higher entropy difference between the amorphous and crystallized states, implying

that as the wheel speed increases, the crystallization process becomes harder, and more ordering energy is required for the phase nucleation.^[24]

The crystallized volume fraction α_{cr} can be calculated by using the fractional area of the exothermic peak in the DSC curve (Equation 2):

$$\alpha_{cr} = \frac{\int_{T_0}^T \left(\frac{dH_c}{dT} \right) dT}{\int_{T_0}^{T_\infty} \left(\frac{dH_c}{dT} \right) dT} \quad (2)$$

where T_0 and T_∞ are crystallization's onset and mindset temperatures, respectively. dH/dT is the heat flow at constant pressure. In Figure 5, the crystallization fraction is plotted against the temperature for MG1, MG2, and MG3 glassy alloys. All curves possess a characteristic sigmoidal shape, which indicates nucleation and growth are taking place. At the beginning of curves, nucleation dominates. As the temperature increases, an increase in the volume fraction of crystalline phases is observed due to the growth of primary nuclei and the nucleation of new ones. However, the dominant phenomenon in this region is the growth process. As temperatures continue to rise, the majority

Table 2. Thermal and magnetic properties of as-cast and annealed MG1, MG2, and MG3 metallic glass microfibers.

Sample/Parameter	T_c	μ_r	M_s	H_c	T_x	T_p
Unit	[K]		[emu]	[Oe]	[K]	[K]
MG1	750	15.6	110	3.5	679	696
MG2	750	14.8	100	4	687	695
MG3	750	4.25	50	3	684	696
MG1-annealed	750	24	83	5.4	*	*
MG2-annealed	750	19	136	4.5	*	*
MG3-annealed	750	16	75	6.5	*	*

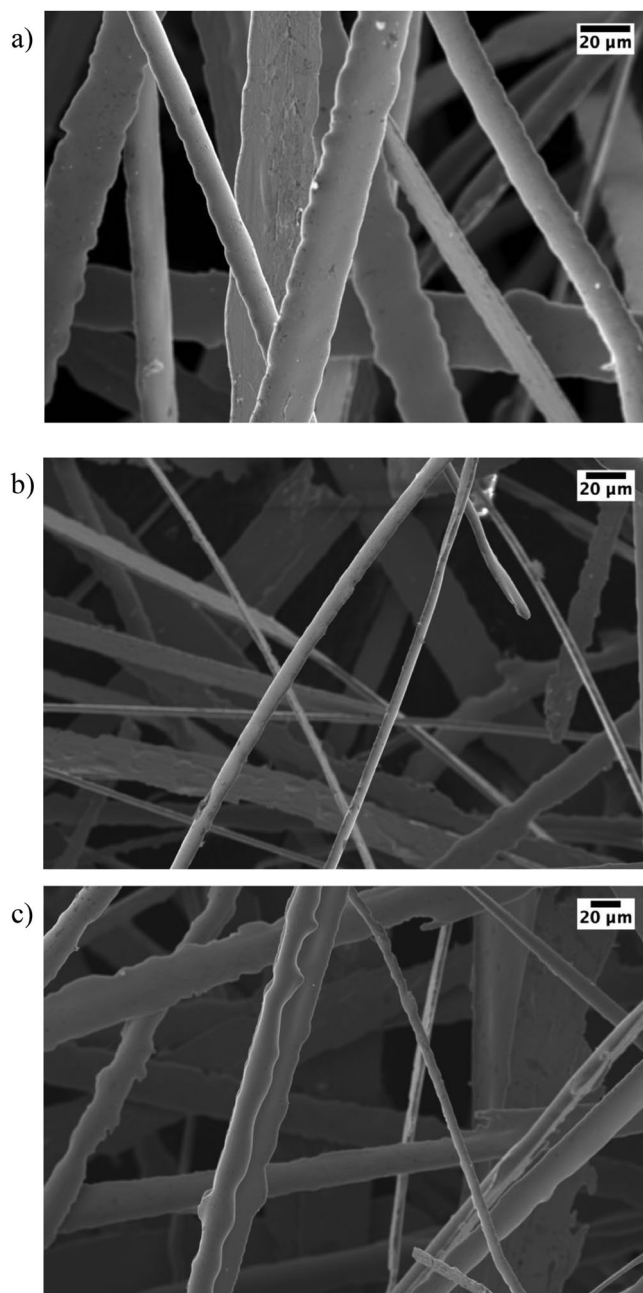


Figure 3. SEM images of $\text{Fe}_{40}\text{Ni}_{40}\text{B}_{20}$ microfibers fabricated by modified melt-spinning technique applying different wheel velocities; a) MG1, b) MG2, c) MG3.

of glassy alloys are crystallized, and the transformation is again sluggish.

Figure 6 shows the temperature and field dependence of magnetization (M) of all samples studied at 0.1 T. The samples were measured during the warm-up cycle after field cooling. A systematic decrease of magnetization of the microfibers is observed as a function of increasing temperature, and the ferromagnetic phase to the paramagnetic phase transition is observed in all the samples slightly close to exact temperature. Curie temperature (T_C) was defined as the peak position in the $dM/dT-T$ curves, as

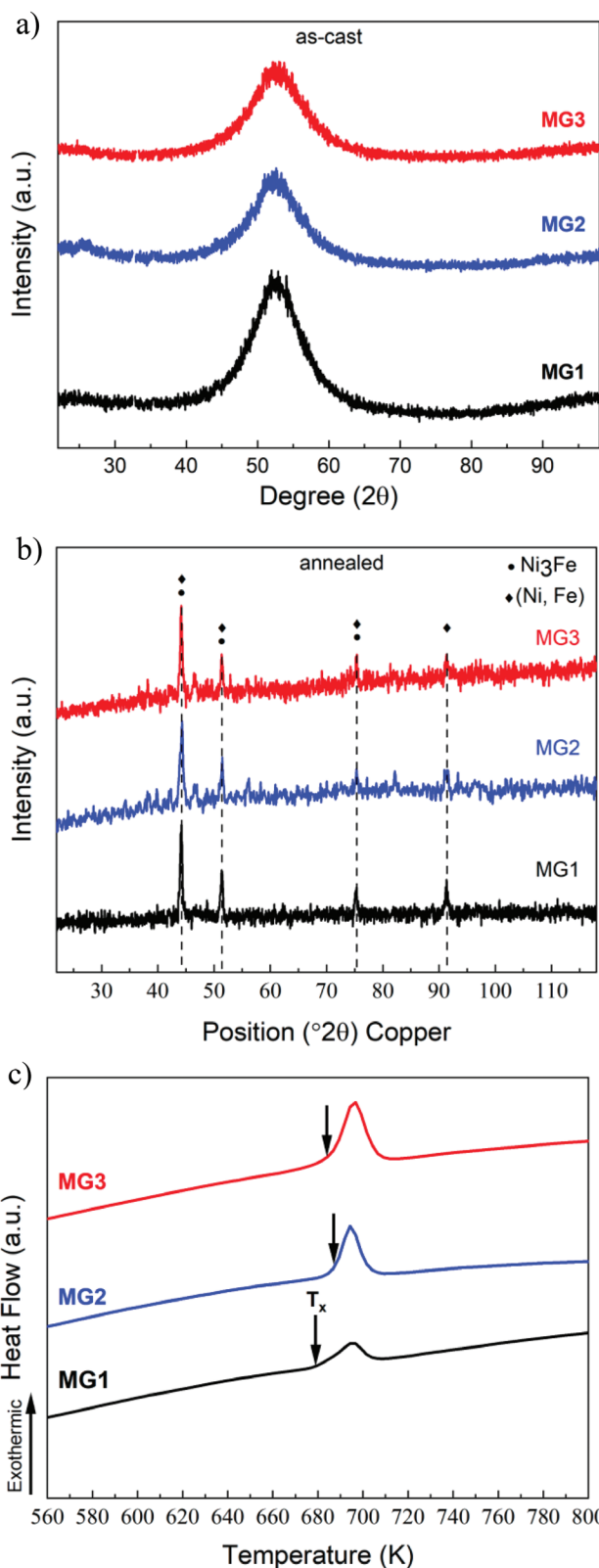


Figure 4. a) XRD analysis on as-cast $\text{Fe}_{40}\text{Ni}_{40}\text{B}_{20}$ microfibers batches MG1, MG2, and MG3. b) XRD analysis on $\text{Fe}_{40}\text{Ni}_{40}\text{B}_{20}$ microfibers after heating up to 800 K, heating rate 10 K min^{-1} . c) DSC analysis on $\text{Fe}_{40}\text{Ni}_{40}\text{B}_{20}$ microfibers.

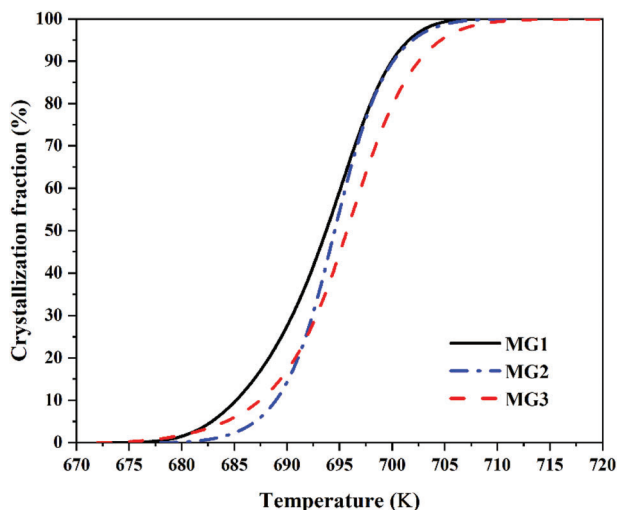


Figure 5. Crystallized volume fraction as a function of temperature for MG1, MG2, and MG3 samples.

shown in the inset in Figure 6. It equals close to 750 K for all samples.

Several articles reported the values of T_c for $\text{Fe}_{40}\text{Ni}_{40}\text{B}_{20}$ alloy, T_c was found to be equal to 680 K,^[18] and 733 K.^[39] As can be seen from this comparison, the T_c values of our samples are close to the reported values.

The transition from an amorphous to a crystalline alloy (Figure 6b) started close to 680 K, in magnetic measurement for all samples. In Figure 6a, an unusual increase in saturation magnetization with temperature from 670 to 691 K is observed. The first step of devitrification mainly was connected with the formation of some crystalline metastable phases as $(\text{Fe,Ni})_3\text{B}$,^[40] $\gamma\text{-FeNi}$,^[41] etc. The first peak (Figure 6b) corresponds to the crystallization of orthorhombic $(\text{Fe,Ni})_3\text{B}$ and the second is linked with rise in $\gamma\text{-FeNi}$ phase.^[39,42] Magnetic measurements show characteristic temperatures close to the same temperature observed at the DSC signal.

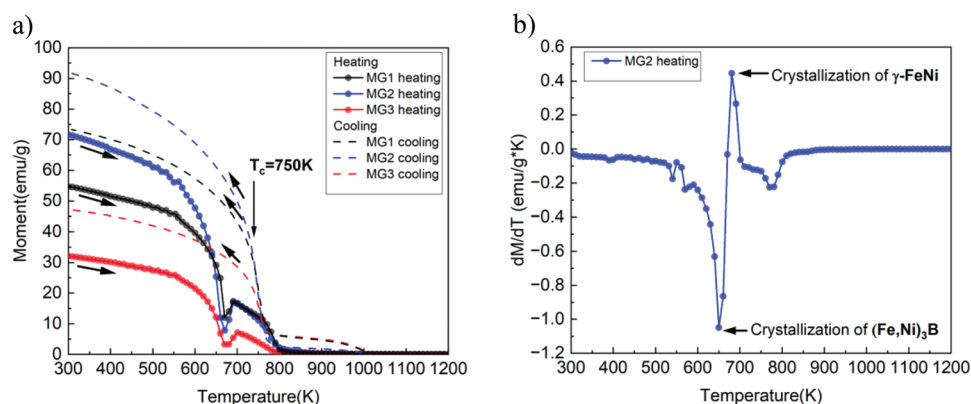


Figure 6. a) The temperature-dependent magnetic behaviors of MG1, MG2, and MG3 alloys during heating and cooling b) Derivative of the temperature dependence for MG2 during heating mode.

Figure 7 shows the magnetization against the applied magnetic field hysteresis loop for $\text{Fe}_{40}\text{Ni}_{40}\text{B}_{20}$ microfibers before and after annealing at the temperature of 800 K. All samples exhibit an ultra-soft magnetic behavior consisting of a hysteresis loop with a saturation magnetization (M_s) in the range of 50–140 emu and coercivities (H_c) in the range of 3–6 Oe.

Coercivity decreases if the sample gets relaxed, it increases if it gets crystallized. The values of M_s and H_c are listed in Table 2. As can be seen, the annealed samples show a higher saturation magnetization compared to the as-cast amorphous samples. The same trend has been seen in the case of remanent magnetization. Among all the samples, after annealing, the MG3 has the most change (intensification) in the magnetic parameters.

Since all samples showed similar magnetic properties, but annealed MG2 exhibited the highest magnetization in low fields, further studies were conducted on the embedded MG2 microfibers inside the epoxy resin, referred to as the epoxy-based composite. The high-frequency characterization of epoxy-based composites is shown in the first panel of **Figure 8**. The sample indicates very high conductivity due to the metallic inclusions and an increased real part of the permittivity with respect to that of the polymeric matrix ($\epsilon' \approx 3.5$). The attenuation constant of the composite is 20–25 times larger than that of the matrix and increases slightly with frequency. The value of the attenuation constant α can then be used to estimate the absorption contribution to the shielding efficiency ($SE_A = 8.868\alpha t$) for an infinite slab of thickness t .^[43] This contribution is usually the dominant one for the total shielding efficiency and is a good measure of the performance of the material for high-frequency attenuation. We find for the FeNiB composite an excellent SE_A that ranges 37.5 dB at 2 GHz to 77.9 at 14 GHz when a thickness of 1 cm is considered.

The measurement of the magnetic flux density in the center of the two tubular arrangements of MG2 microfibers allowed the evaluation of their static magnetic field shielding efficiency via the evaluation of the shielding factor (SF), defined as the ratio between the applied magnetic field and the measured magnetic flux density ($SF = B_{app}/B_z$).^[43]

All the measurements indicate an anisotropic behavior of both the shield arrangements according to the microfibers anisotropic

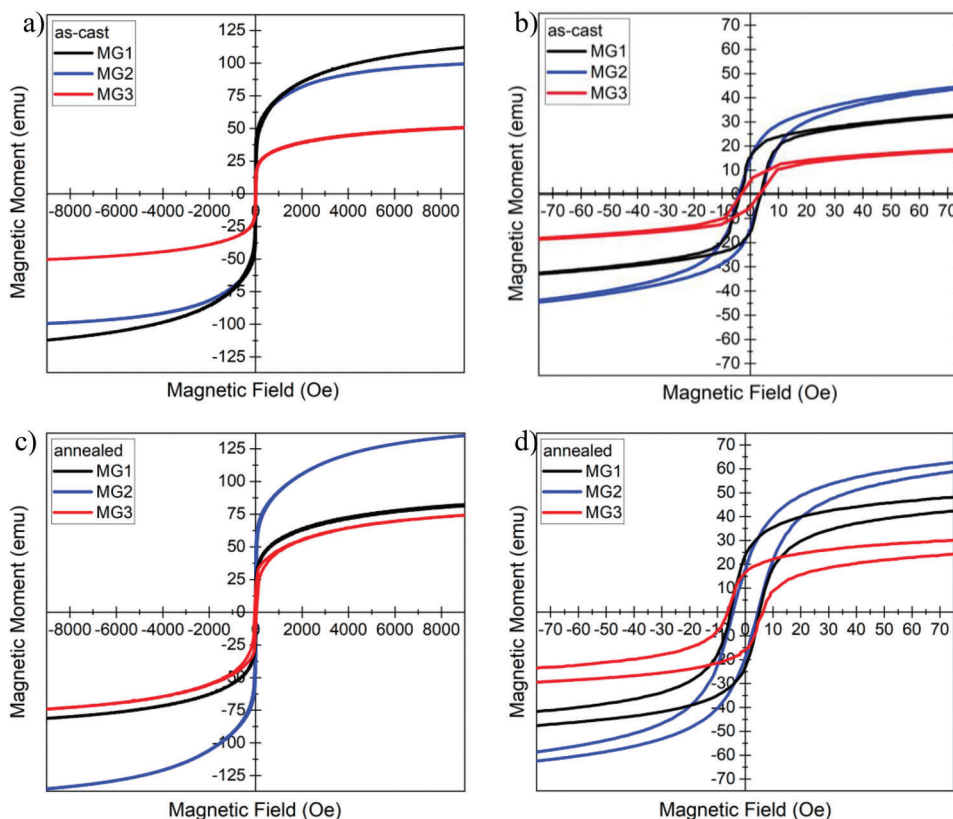


Figure 7. Hysteresis loops for as-cast and annealed MG1, MG2, and MG3 alloys at a high magnetic field (a,c), and low magnetic field (b,d).

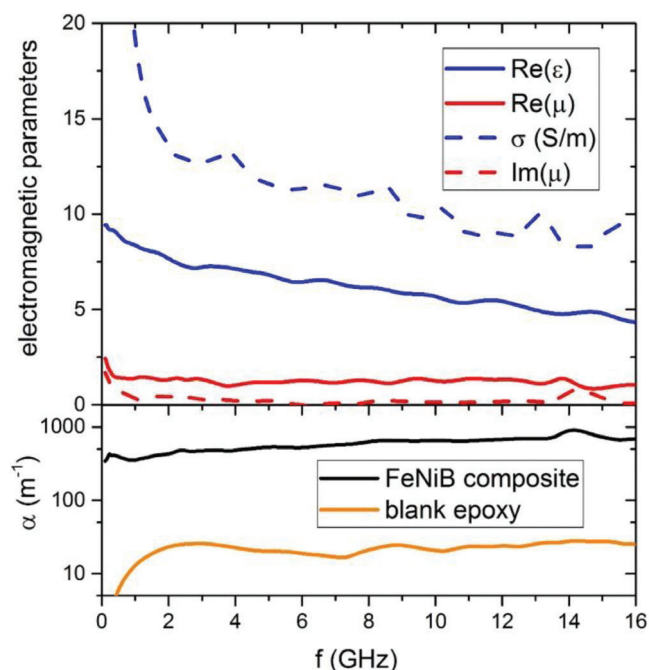


Figure 8. Top panel: high-frequency electromagnetic properties of the MG2 microfibers embedded in an epoxy matrix. Bottom panel: attenuation coefficient of electromagnetic radiation of the MG2 composite sample (black) compared to the blank epoxy matrix (orange).

behavior. Indeed, the shielding performances are greater when the microfiber orientations and the applied magnetic field are placed on the same plane/direction. For the MG2 vertical configuration, an SF > 3 is reached in the axial field orientation (Figure 9b red curve), while an SF = 2 is obtained in the transverse one (Figure 9d red curve). Conversely, with the MG2 horizontal configuration using a transverse applied magnetic field an SF > 4.5 is gained, which falls to SF ≈ 1.5 in axial field configuration (Figure 9d and Figure 9b black curve).

However, the values of SF could be affected by the different number of microfibers used to assemble the shields, i.e. by the mass of the shield. For this reason, when a mass normalized values of the SFs are considered, SF = 7.1 g⁻¹ and SF = 4.1 g⁻¹ are found for the MG2 vertical in axial and transverse field respectively, while SF = 2 g⁻¹ is obtained for the MG2 horizontal in axial field and SF = 6.1 g⁻¹ in transverse field orientation.

The shielding performance remains substantial for an applied magnetic field lower than 20 Oe, corresponding to the region of high susceptibility values shown in Figure 7b. However, above the applied field $B_{app} = 65$ Oe, the shielding factor curve can be considered flat and close to unity in both the orientations and for all the shields. The shielding measurements confirm the ultra-soft magnetic behaviour of the fibers with a negligible residual magnetic flux density field near the center of the shield.

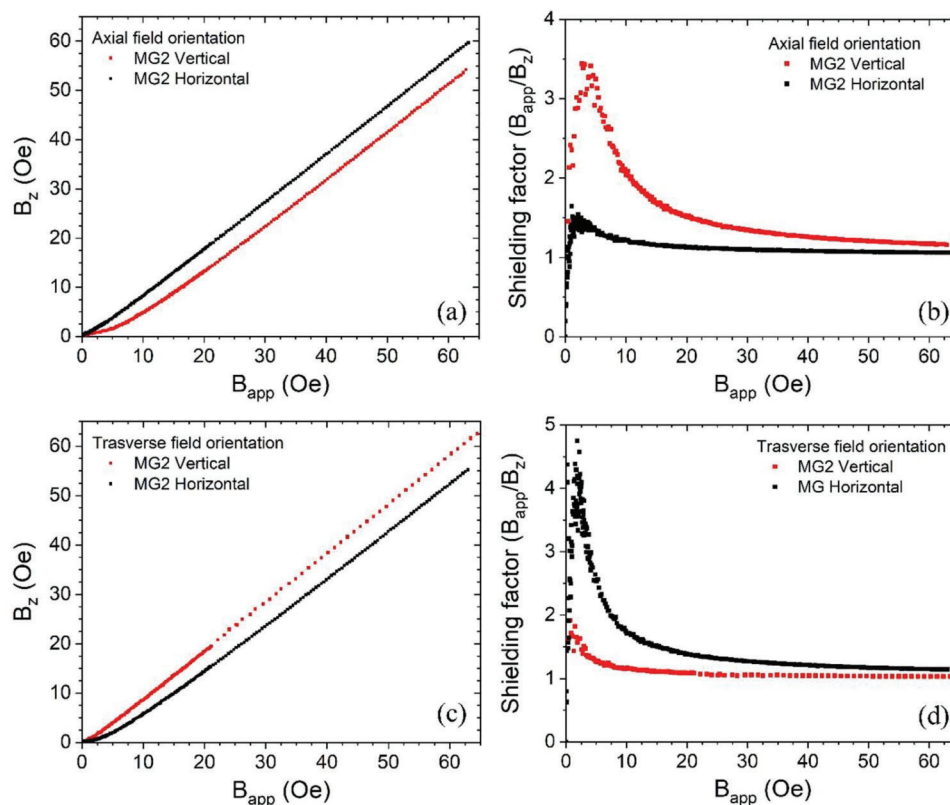


Figure 9. The magnetic flux density of MG2 microfibers measured by the Hall probe positioned at the center of the tubular shield (a,c) and corresponding shielding factor for the two microfibers arrangements (b,d). The measurement was performed in the axial field (panels a,b) and transverse (panels c,d) orientation.

4. Conclusion

In this study, we employed a custom-designed melt-spinning technique with three different wheel linear velocities: 51.02 to 59.66 m s⁻¹, and 62.8 m s⁻¹.

- The fabricated Fe₄₀Ni₄₀B₂₀ metallic glass microfibers had a 5 μm diameter.
- XRD analysis confirmed the fully amorphous structure of all three samples, while DSC analysis showed almost identical characteristic temperatures of T_g and T_x . The DSC analysis also showed a single endothermic peak at ≈700 K for all three curves, which could be associated with the eutectic crystallization of γ -Fe-Ni and (Fe,Ni)₃B phases.
- The area under the crystallization peak indicated that increasing the wheel velocity from 51.02 to 59.66 m s⁻¹ and 62.8 m s⁻¹ led to a change in crystallization enthalpy from 48 μV s⁻¹ mg⁻¹, to 62 μV s⁻¹ mg⁻¹, and 213 μV s⁻¹ mg⁻¹, respectively.

It is noteworthy that the temperature range for crystallization of all samples was similar to that observed in the DSC analysis. Furthermore, by monitoring the phase formation based on the magnetic signal using the VSM method, it was possible to distinguish the nucleation event of both crystalline phases: (Fe,Ni)₃B and γ -Fe-Ni.

The microfibers displayed anisotropic static field shielding behavior that corresponded to their anisotropic nature, with the best shielding performance observed when the magnetic field was aligned with the fibers. At GHz frequencies, embedding the microfibers in an epoxy matrix resulted in 20–25 times increase in the composite's attenuation constant.

Acknowledgements

E.S. would like to thank KMM-VIN for providing funding for this project. The research results presented in this paper have been developed with the use of equipment financed from the funds of the “Excellence Initiative – Research University” program at AGH University of Science and Technology.

Conflict of Interest

The authors declare no conflict of interest.

Author Contributions

E.S. contributed to the conceptualization, methodology, and writing original draft; A.Ż. contributed to magnetic measurements; B.S. contributed to the discussion and reviewing manuscript; T.K. contributed to the metallic microfiber fabrication; R.R. contributed to methodology and writing original draft; P.B. contributed to methodology, validation and reviewing

manuscript; D.T., G.G., and R.G. contributed to high-frequency characterization, to the discussion, and to the writing of the manuscript; M.F., and L.G. contributed to magnetic shielding measurements, to the discussion, and to the writing of the manuscript.

Data Availability Statement

The data that support the findings of this study are available from the corresponding author upon reasonable request.

Keywords

electromagnetic shielding, low coercivity, metallic glass, microfibers, soft magnetic properties, wearable electronics

Received: March 17, 2023

Revised: May 7, 2023

Published online:

- [1] Z. Li, Z. Huang, F. Sun, X. Li, J. Ma, *Mater. Today Adv.* **2020**, *7*, 100077.
- [2] J. Schroers, T. M. Hodges, G. Kumar, H. Raman, A. J. Barnes, Q. Pham, T. A. Waniuk, *Mater. Today* **2011**, *14*, 14.
- [3] B. Zheng, Y. Zhou, J. E. Smugersky, E. J. Lavernia, *Metall Mater Trans A Phys Metall Mater Sci* **2009**, *40*, 1235.
- [4] H. Liu, Q. Jiang, J. Huo, Y. Zhang, W. Yang, X. Li, *Addit. Manuf.* **2020**, *36*, 101568.
- [5] J. Liu, X. Wang, Z. Li, Y. Zhang, G. Cao, M. Huang, H. Shen, *Mater. Today Commun.* **2019**, *20*, 100605.
- [6] J. Liu, M. Huang, M. Wu, Y. Zhang, G. Cao, Z. Li, H. Chen, T. Yu, X. Wang, R. Liu, G. Qu, M. Pang, H. Shen, *J. Alloys Compd.* **2021**, *855*, 157231.
- [7] M. Hagiwara, A. Inoue, T. Masumoto, *Metall. Trans. A* **1982**, *13*, 373.
- [8] M. Hagiwara, A. Inoue, T. Masumoto, *Mater. Sci. Eng.* **1982**, *54*, 197.
- [9] J. Liu, Y. Wang, G. Qu, R. Liu, Y. Zhang, C. Wang, *Met.* **2022**, *12*, 2041.
- [10] M. Zhang, G. Qu, J. Liu, M. Pang, X. Wang, R. Liu, G. Cao, G. Ma, *Mater.* **2021**, *14*, 3589.
- [11] C. Zhu, J. Wu, J. Yan, X. Liu, *Adv. Fiber Mater.* **2022**, *5*, 12.
- [12] S. Jagdale, A. Javed, S. Theeda, C. S. Meduri, Z. Hu, M. Hasan, G. Kumar, **2022**, *12*, 518.
- [13] S. Mohanty, M. Geetha, in *Nanofiber Composites for Biomedical Applications* (Eds: M. Ramalingam, S. Ramakrishna), Elsevier Inc., Sawston, UK **2017**, pp. 79–94.
- [14] E. Sharifikolouei, B. Sarac, Y. Zheng, P. Bala, J. Eckert, *Sci. Rep.* **2022**, *12*, 10784.
- [15] E. Sharifikolouei, B. Sarac, A. Micoulet, R. Mager, M. Watari-Alvarez, E. Hadjixenophontos, Z. Burghard, G. Schmitz, J. P. Spatz, *Mater. Des.* **2022**, *223*, 111242.
- [16] H. Chen, B. Dong, S. Zhou, X. Li, J. Qin, *Sci. Rep.* **2018**, *8*, 4.
- [17] I. Chicanas, V. Pop, O. Isnard, *J. Magn. Magn. Mater.* **2002**, *242–245*, 885.
- [18] M. Kadziołka-Gaweł, W. Zarek, E. Popiel, A. Chrobak, *Acta Phys Pol A* **2010**, *117*, 412.
- [19] A. Rauf, Y. Fang, H. Zhang, G. Peng, T. Feng, *J. Non Cryst Solids* **2019**, *521*, 119500.
- [20] G. Pookat, H. Thomas, S. Thomas, S. H. Al-Harhi, L. Raghavan, I. A. Al-Omari, D. Sakthikumar, R. V. Ramanujan, M. R. Anantharaman, *Surf. Coatings Technol.* **2013**, *236*, 246.
- [21] A. Inoue, H. Koshiba, T. Zhang, A. Makino, *Mater. Trans. JIM.* **1997**, *38*, 577.
- [22] A. Inoue, T. Zhang, T. Itoi, A. Takeuchi, *Mater. Trans. JIM.* **1997**, *38*, 359.
- [23] P. Ohodnicki, J. Egbu, Y. Yu, J. Baltrus, N. Aronhime, Y. Krimer, P. Anand, K. Byerly, M. E. McHenry, *J. Alloys Compd.* **2020**, *834*, 155038.
- [24] J. Zhou, W. Yang, C. Yuan, B. Sun, B. Shen, *J. Alloys Compd.* **2018**, *742*, 318.
- [25] T. Wang, J. Chen, R. Wei, C. Chen, F. Li, *J. Mater. Sci.* **2021**, *32*, 21206.
- [26] C. Liang, C. P. Gooneratne, Q. X. Wang, Y. Liu, Y. Gianchandani, J. Kosel, *Biosensors.* **2014**, *4*, 189.
- [27] F. L. Kong, C. T. Chang, A. Inoue, E. Shalaan, F. Al-Marzouki, *J. Alloys Compd.* **2014**, *615*, 163.
- [28] J. Zhou, Q. Wang, X. Hui, Q. Zeng, Y. Xiong, K. Yin, B. Sun, L. Sun, M. Stoica, W. Wang, B. Shen, *Mater. Des.* **2020**, *191*, 108597.
- [29] Y. Okazaki, K. Ueno, *J. Magn. Magn. Mater.* **1992**, *112*, 192.
- [30] M. Yamaguchi, Y. Miyazawa, K. Kaminishi, H. Kikuchi, S. Yabukami, K. I. Arai, T. Suzuki, *J. Magn. Magn. Mater.* **2004**, *268*, 170.
- [31] L. Wang, S. Chen, X. Sun, J. Chen, J. Liang, M. Wang, *Addit. Manuf.* **2022**, *55*, 102811.
- [32] T. W. Shyr, J. W. Shie, *J. Magn. Magn. Mater.* **2012**, *324*, 4127.
- [33] J. Lee, B. M. Jung, S. B. Lee, S. K. Lee, K. H. Kim, *Appl. Surf. Sci.* **2017**, *415*, 99.
- [34] D. Ba, P. Sabouroux, *Microw Opt Technol Lett* **2010**, *52*, 2643.
- [35] D. Torsello, G. Ghigo, M. Giorcelli, M. Bartoli, M. Rovere, A. Tagliaferro, *Carbon Trends* **2021**, *4*, 100062.
- [36] A. M. Nicolson, G. F. Ross, *IEEE Trans. Instrum. Meas.* **1970**, *19*, 377.
- [37] J. Baker-Jarvis, E. J. Vanzura, W. A. Kissick, *IEEE Trans Microw Theory Tech* **1990**, *38*, 1096.
- [38] B. Zhao, G. Shao, B. Fan, W. Zhao, Y. Chen, R. Zhang, *RSC Adv.* **2015**, *5*, 9806.
- [39] P. Allia, M. Baricco, P. Tiberto, F. Vinai, *Phys Rev B* **1993**, *47*, 3118.
- [40] F. Maccari, D. Y. Karpenkov, E. Semenova, A. Y. Karpenkov, I. A. Radulov, K. P. Skokov, O. Gutfleisch, *J. Alloys Compd.* **2020**, *836*, 155338.
- [41] K. J. Miller, M. Sofman, K. McNerny, M. E. McHenry, *J. Appl. Phys.* **2010**, *107*, 09A305.
- [42] F. Maccari, D. Y. Karpenkov, E. Semenova, A. Y. Karpenkov, I. A. Radulov, K. P. Skokov, O. Gutfleisch, *J. Alloys Compd.* **2020**, *836*, 155338.
- [43] M. Fracasso, F. Gömöry, M. Solovyov, R. Gerbaldo, G. Ghigo, F. Laviano, A. Napolitano, D. Torsello, L. Gozzelino, *Materials* **2022**, *15*, 667.